Experimental Characterization of RF-SQUIDs Based Josephson Traveling Wave Parametric Amplifier Exploiting Resonant Phase Matching Scheme

Experimental Characterization of RF-SQUIDs Based Josephson Traveling Wave Parametric Amplifier Exploiting Resonant Phase Matching Scheme

L. Fasolo, F. Ahrens, G. Avallone, C. Barone, M. Borghesi, L. Callegaro, G. Carapella, A. P. Caricato, I. Carusotto, A. Cian, A. D'Elia, D. Di Gioacchino, P. Falferi, M. Faverzani, E. Ferri, G. Filatrella, C. Gatti, D. Giubertoni, V. Granata, C. Guarcello, D. Labranca, A. Leo, C. Ligi, P. Livreri, G. Maccarrone, F. Mantegazzini, B. Margesin, G. Maruccio, R. Mezzena, A. G. Monteduro, R. Moretti, A. Nucciotti, L. Oberto, L. Origo, S. Pagano, A. S. Piedjou, L. Piersanti, A. Rettaroli, S. Rizzato, S. Tocci, A. Vinante, M. Zannoni, A. Giachero, and E. Enrico

***Abstract*—This study presents recent advancements in Josephson Traveling Wave Parametric Amplifiers (JTWPAs) developed and tested at Istituto Nazionale di Ricerca Metrologica within the Detector Array Readout with Traveling Wave AmplifieRS project framework. Combining Josephson junctions with superconducting coplanar waveguides, JTWPAs offer advanced capabilities for quantum-limited broadband microwave amplification and the emission of non-classical microwave radiation. The work delves into the architecture, optimization, and experimental characterization of a JTWPA with a Resonant Phase-Matching mechanism, highlighting signal gains and idler conversion factors in relation to pump power and signal frequency.**

***Index Terms*—Josephson devices, parametric amplifiers, superconducting microwave devices, superconducting resonators.**

I. Introduction

In THIS paper, we present recent advances on Josephson Traveling Wave Parametric Amplifiers [1], [2] (JTWPAs) developed and tested at the Istituto Nazionale di Ricerca Metrologica (INRiM) within the Detector Array Readout with Traveling Wave AmplifieRS (DARTWARS) project [3], [4], [5], [6], [7], [8], [9], [10]. JTWPAs are engineered metamaterials composed of a repetition of several hundreds of Josephson junctions embedded in a superconducting coplanar waveguide. The Josephson junctions confer to the material a non-linear behavior and promote a medium-mediated energy exchange, known as parametric down-conversion, between a strong propagating microwave pump tone (f_p) and a couple of energy-preserving weak tones, called respectively signal (f_s) and idler (f_i). This working principle makes the JTWPAs both an important tool for the quantum-limited broadband microwave amplification and for the emission of non-classical microwave radiation, being the signal and idler tones composed of entangled photons. The latter can be exploited in a wide variety of quantum sensing techniques such as quantum illumination [11], and quantum key distribution [12].

In particular, we here present the architecture of an Al/AlOx/Al rf-SQUID-based JTWPA [13], [14] equipped with a Resonant Phase-Matching (RPM) scheme [15]. The distinctive feature of an ideal rf-SQUID-based JTWPA lies in its ability to operate alternatively in a pure four-wave ($2f_\mathrm{p} = f_\mathrm{s} + f_\mathrm{i}$) or in a pure three-wave mixing regime ($f_\mathrm{p} = f_\mathrm{s} + f_\mathrm{i}$). The shift between these two regimes is obtained by tuning the Josephson inductances with an external bias, such as an external magnetic field or a dc current flowing along the coplanar waveguide. As a side-effect, the inductances variation also causes a change in the impedance of the line, thus requiring a design tailored to the intended operating regime.

JTWPAs operating in three-wave mixing provide a greater amplification at low pump powers compared to those operating in four-wave mixing. For the same reasons, they also necessitate shorter structures to achieve a target amplification, thus introducing fewer losses in the system [16]. Additionally, as the maximum gain is attained at half the pump frequency, this strong driving tone can be easily filtered out without affecting the amplification bandwidth. Despite the large number of theoretical proposals for JTWPAs operating in three-wave mixing [13], [17], [18], [19], the number of effective implementations reported in literature remains limited [16], [20].

The design presented in this paper was developed using a finite element electromagnetic simulator (Sonnet 14.54) [21],

Manuscript received 26 September 2023; revised 22 December 2023 and 19 January 2024; accepted 23 January 2024. Date of publication 29 January 2024; date of current version 27 February 2024. This work was supported in part by DARTWARS, a project funded by the European Union's H2020-MSCA under Grant 101027746, in part by the Italian Institute of Nuclear Physics (INFN), within the Technological and Interdisciplinary Research Commission (CSN5), in part by the Italian National Quantum Science and Technology Institute through the PNRR MUR Project under Grant PE0000023- NQSTI. The work of E. Enrico, L. Fasolo, L. Callegaro, and L. Oberto was supported in part by the European Project SuperQuant and in part by the European Union's Horizon 2020 Research and Innovation Programme under Grant 863313 (SUPERGALAX). The project 20FUN07 SuperQuant has received funding from the EMPIR programme co-financed by the Participating States and from the European Union's Horizon 2020 research and innovation programme. The work of S. Pagano and C. Barone was supported in part by the University of Salerno - Italy under Projects FRB19PAGAN, FRB20BARON, and FRB22PAGAN. *(Corresponding author: L. Fasolo.)*

Please see the Acknowledgment section of this article for the author affiliations.

Color versions of one or more figures in this article are available at https://doi.org/10.1109/TASC.2024.3359163.

Digital Object Identifier 10.1109/TASC.2024.3359163

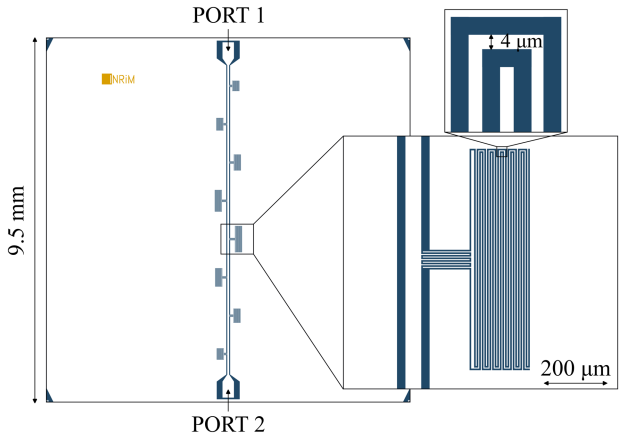

Fig. 1. Layout of the device containing eight compact planar LC resonators capacitively and inductively coupled to a single feed line. The design of each resonator is such as to generate a unique resonance frequency. The white layer represents the patterned aluminum film.

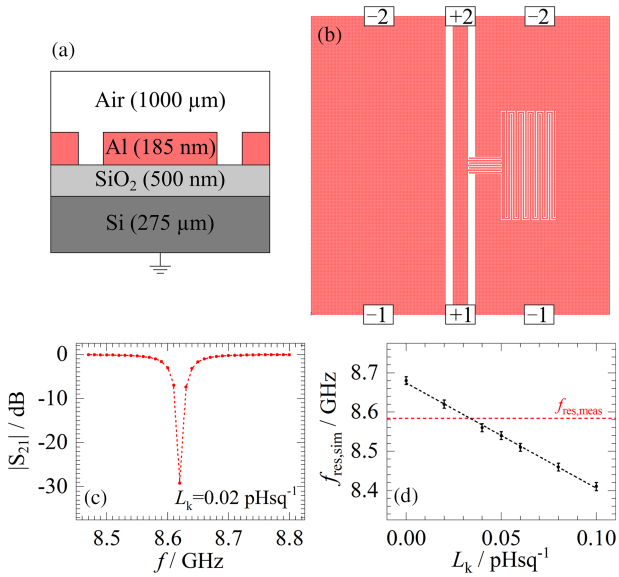

Fig. 2. (a) Stack of the materials modeled in the electromagnetic simulations. (b) Layout implemented in Sonnet for the simulation of the $|S_{21}|$ of the feed line coupled to an LC resonator. (c) Results of one of the simulations represented in terms of a $|S_{21}|$ spectrum in the specific case of an aluminum thin film having a kinetic inductance $L_k = 0.02\,\mathrm{pHsq}^{-1}$. (d) Linear fit of the simulation-extracted resonant frequencies ($f_{res,sim}$) for different values of the kinetic inductance and comparison with the measured resonance frequency ($f_{res,meas}$).

to specifically optimize the performance of the parametric amplifier when operating in the three-wave mixing regime. The layout is aimed to address common issues in such a class of devices [22], such as the unwanted internal reflections resulting from impedance mismatches between different segments of the device, as well as the energy dispersion in higher harmonics and up-conversion products. This latter is handled by exploiting an RPM scheme based on compact planar LC resonators.

Section II reports the outcomes of a simulation and measurement campaign aimed at evaluating the exploitability of superconducting planar LC resonators with a reduced footprint in an RPM-JTWPA. Based on these propaedeutic results, Section III presents the design and the preliminary cryogenic characterization of an rf-SQUID-based JTWPA equipped with an RPM scheme and with a desired amplification bandwidth center around 8.5 GHz. The performance of the realized device has been quantified in terms of signal gain, idler conversion factor, and bandwidth, all estimated by means of the pump-on-pump-off technique.

II. Resonant Phase-Matchers Optimization

To optimize the layout of compact planar LC resonators suitable for integration into RPM-JTWPAs in terms of frequency targeting, a dedicated test device was designed and simulated with finite-element electromagnetic simulations. The simulation results, expressed in terms of $|S_{21}|$ spectra, were subsequently compared to the experimental results obtained with cryogenic measurements ($T = 75$ mK) on the fabricated device. The test device (see Fig. 1), made of a central feed line coupled to 8 different resonators, each with a unique resonance frequency in the 4–12 GHz range, was fabricated by utilizing a standard aluminum lift-off process based on a UV-lithography on a 275 µm-thick p-doped silicon wafer covered with 500 nm of thermal oxide. The comparison of experimental and simulation results was additionally employed to extrapolate an estimation of the kinetic inductance L_k per unit surface for the $t = 185$ nm-thick evaporated aluminum film.

As shown in Fig. 1, the LC resonators were designed as hanger-type short-circuited λ/4 resonators, where one of their ends is capacitively and inductively coupled to a feed line, while the other end is shorted to ground. As schematically depicted in Fig. 2(a), the simulations were performed modelling the effective substrate as a stack made of a bottom layer of 275 µm-thick Si (relative dielectric constant $\epsilon_r = 11.9$, tangent loss $\delta = 5 \times 10^{-6}$ and conductivity $\sigma = 4.4 \times 10^{-4}\,\mathrm{Sm}^{-1}$) and a top layer of 0.5 µm-thick SiO_2 ($\epsilon_r = 3.9$, $\delta = 3 \times 10^{-4}$, and $\sigma = 0\,\mathrm{sm}^{-1}$) [23]. Furthermore, the superconducting Al thin-film was treated as a resistive-less material with a parameterized kinetic inductance assuming 7 different values in the 0–0.1 pHsq^{-1} range. As depicted in Fig. 2(b), the behaviour of each of the 8 resonators was separately simulated fixing the mesh of the sub-sectioning of the patterned structure to 1 μm^2, four times smaller than the smallest device detail, while the $|S_{21}|$ scattering parameter of the feed line was evaluated with a frequency step of 10 MHz. As an example, Fig. 2(c) reports the output of the electromagnetic simulation performed on the layout presented in Fig. 2(b) in the case of $L_k = 0.02\,\mathrm{pHsq}^{-1}$.

From each of the simulated responses, the resonance frequency $f_{res,sim}$ was determined as the frequency at which the lowest $|S_{21}|$ value was obtained. These resonance frequencies were then plotted against the kinetic inductance of the metallic layer. As an example, Fig. 2(d) presents the results of this mapping for one of the resonators. In this graph, the error bar has been sized to the simulation step size (10 MHz). For all the 8 analyzed structures, the relationship between resonance frequency and kinetic inductance can be approximated as linear within the range of low kinetic inductance considered.

By averaging the 8 kinetic inductances extrapolated from the comparison of the 8 separate linear fits with the respective measured resonant frequencies ($f_{res,meas}$), it can be concluded that the t =185 nm-thick aluminum film under test shows, at T = 75 mK, a kinetic inductance $L_k = (0.050 \pm 0.015)\,\mathrm{pHsq}^{-1}$,

where the uncertainty on the extrapolated value is obtained from the mean standard deviation of the 8 different obtained results.

This result can be compared with the theoretical prediction derived from the London superconducting theory [24] when considering a superconducting strip of thickness t cooled at a temperature T well below its critical value ($T \ll T_c$). For such a structure, the normalized kinetic inductance per unit of transverse area of the strip is reported to be:

$$L_k(t) = \frac{\mu_0 \lambda_0(t)}{4}\left[\coth\left(\frac{t}{2\lambda_0(t)}\right) + \frac{t}{2\lambda_0(t)}\csc^2\left(\frac{t}{2\lambda_0(t)}\right)\right], \tag{1}$$

where μ_0 is the vacuum magnetic permeability and $\lambda_0(t)$ is the London penetration depth, which is a function of the film thickness. The kinetic inductance extracted from the comparison between simulation and measurements is in agreement with the value predicted by (1) when considering $\lambda_0(t = 185\ \text{nm}) \approx 65$ nm. Investigating the properties of the deposited aluminum thin films in further detail would have necessitated performing measurements on resonators with different film thicknesses. However, this level of extensive analysis falls outside the scope of this work. In Section III, the results obtained were used as a first-level approximation to model the kinetic inductance contribution of the patterned aluminum thin film to the S_{21} parameter.

The experimental measurement of the test device also allowed for the evaluation of the suitability of the compact LC planar resonators for implementing an RPM scheme, particularly in terms of their quality factor. Indeed, a noteworthy property of the hanger-type resonators is that their characteristics can be fully determined by measuring the loaded $|S_{21}|$ of the feed line to which they are coupled. Around each resonance frequency f_{res}, this latter quantity can be expressed in terms of the quality factors of the corresponding resonator as follows [25], [26]:

$$|S_{21}(f)| = \left|A\left(1 + \alpha\frac{f - f_{res}}{f_{res}}\right)\left(1 - \frac{Q_l/Q_e}{1 + 2iQ_l\frac{f - f_{res}}{f_{res}}}\right)\right|, \tag{2}$$

where A is the transmission amplitude far from the resonance, corrected for a linear dependency on the frequency through the factor α. Q_l is the loaded quality factor of the resonator, which encompasses both the intrinsic losses of the resonator, quantified by the internal quality factor Q_i, and the external losses resulting from its coupling with the environment, quantified by the coupling quality factor Q_c. This latter quantity is related to the complex-valued external quality factor $Q_e = |Q_e|\exp(-i\theta)$, in which the imaginary part takes into account impedance mismatches in the feed line, resulting in asymmetries in the $|S_{21}|$ spectrum near the resonant frequency. The relationship between the coupling quality factor and the external quality factor is given by $1/Q_c = \text{Re}(1/Q_e)$. Loaded, intrinsic, and coupling quality factors are related as follows:

$$\frac{1}{Q_l} = \frac{1}{Q_i} + \frac{1}{Q_c}. \tag{3}$$

Fig. 3 illustrates, as an example, the response of two of the resonators coupled to the feedline for 3 different input powers. It can be noticed from Fig. 3 that the width of these two representative peaks changes with the excitation power of the

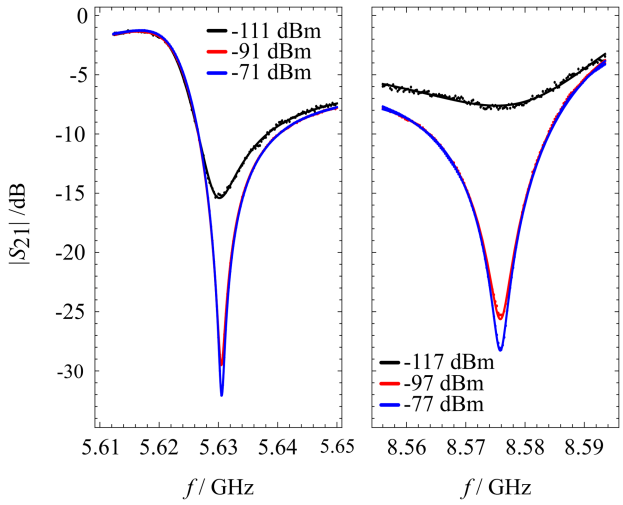

Fig. 3. $|S_{21}|$ scattering parameter of the feed line in the proximity of the resonant frequencies of two of the coupled resonators. The measures were performed at a base temperature of 75 mK and are presented for three different input powers at the DUT.

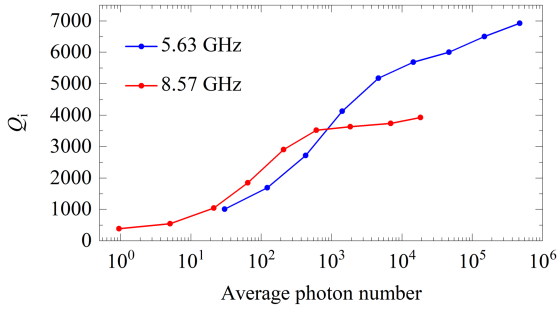

Fig. 4. Internal quality factors extracted from the fit of the measured $|S_{21}|$ near the resonance frequencies 5.63 GHz and 8.75 GHz as a function of the average photon number occupying the resonators.

resonators. The dependency of the measured internal quality factor Q_i from the probing power P, this latter expressed in terms of the average number of photons occupying the resonator ($\langle n \rangle = (P/\pi h f_{res}^2) \cdot (Q_l^2/Q_c)$), is presented in Fig. 4. This power dependency is qualitatively in accordance with two-level system (TLS) losses, as reported in [27], [28], which is typically the main source of losses in planar resonators. All the analyzed resonators showed, in this power range, an internal quality factor lower than 10^5, which is at least three orders of magnitude lower than state-of-the-art resonators [29]. One of the factors contributing to the relatively low quality factors is the compact size of the resonators. Indeed, compact LC resonators have been shown to have a higher sensitivity to losses [28]. This is because the more concentrated electromagnetic fields in compact resonators can couple more strongly with loss sources located in the surrounding materials. Nevertheless, the relatively low quality factor of such compact resonators is not problematic for the implementation of an RPM scheme in JTWPAs. On the contrary, it has been demonstrated that resonators with a lower quality factor exhibit greater robustness against resonator frequency spread. This latter has been demonstrated to cause

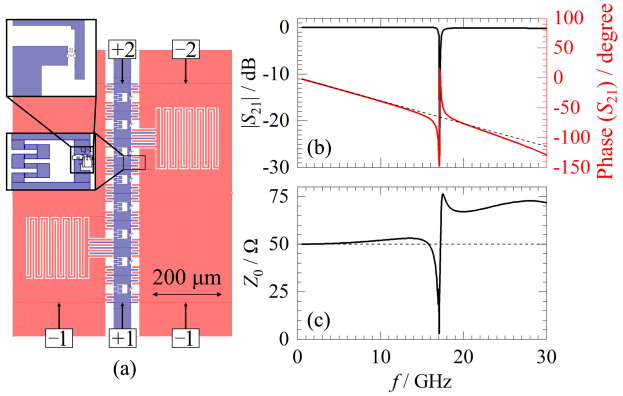

Fig. 5. (a) Representation of the supercell (eight rf-SQUIDs and two LC resonators) simulated in Sonnet. (b) Magnitude and phase of the S_{21} parameter. (c) characteristic impedance Z_0 of the supercell extracted from the finite element simulation.

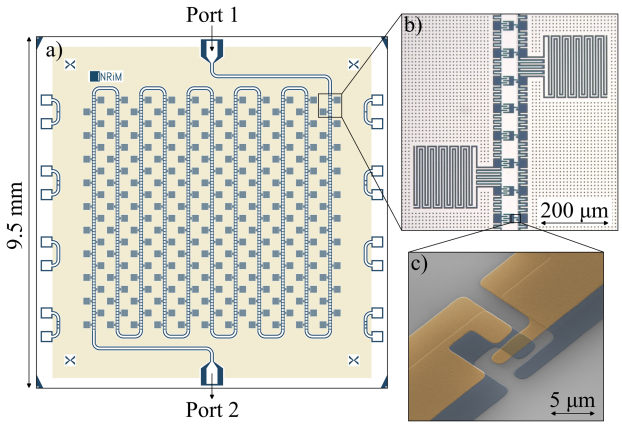

Fig. 6. (a) Physical layout of the complete rf-SQUID-based JTWPA equipped with an RPM scheme. (b) Optical micrograph of one of the supercells composing the fabricated device. (c) False-colored SEM image of one of the Al/Al-Ox/Al Josephson junctions placed along the transmission line.

widened resonances with a reduced ability to distort the dispersion relation and ensure the phase-matching condition between the propagating tones [30].

III. RPM-JTWPA Modeling and Characterization

The physical layout of an RPM-JTWPA, specifically designed to meet the impedance matching condition when operated in the three-wave mixing mode, and to have a bandwidth centered at 8.5 GHz ($f_p = 17$ GHz), was realized starting from the design of a repetition of rf-SQUIDs embedded in a coplanar waveguide with a spatial periodicity of $a = 80$ μm. The layout was optimized by exploiting finite element simulations on a single supercell of the RPM-JTWPA, as reported in Fig. 5(a). The simulation was conducted by modeling the substrate as reported in Section II and taking into account the contribution of the kinetic inductance of the patterned films, according to the results presented in that section. The structure was simulated using a mesh size of 1 μm^2, which was chosen as a compromise between simulation precision and reasonable computational time.

Since the condition of pure three-wave mixing is attained when an external bias drives the Josephson junctions in their divergent state (i.e., when they behave as infinite inductances), these latter were modeled in the electromagnetic simulations as pairs of open-circuit electrodes. Furthermore, their capacitive behavior was incorporated into the simulations by connecting the electrodes with ideal capacitance elements (see insets in Fig. 5(a)). Assuming junctions with an overlapping area of 3.5 μm^2 and a capacitance per unit area of $\rho_C = 60$ fFμm^{-2} [13], these ideal elements were set to $C_J = 210$ fF.

To finalize the design of the rf-SQUIDs, meandered geometrical inductances were introduced in parallel to the junctions. The layout of these elements ($L_g = 46.5$ pH) was selected to create rf-SQUIDs with a resonant frequency of around $2.5 \cdot f_p = 42.5$ GHz. The choice of this frequency was made with the intention of inducing a distortion in the linear high-frequency dispersion relation, thus mitigating the production of higher harmonics of the pump tone and up-conversion products by increasing their phase mismatch. The effect of the distortion of the dispersion relation up to 30 GHz is illustrated in Fig. 5(b), showcasing a deviation of the S_{21} phase from a linear behavior in the high-frequency range. A linear relation was restored around f_p introducing a resonant peak generated through the coupling of the transmission line with an array of hanger-type short-circuited $\lambda/4$ compact LC resonators, located in an alternate pattern, one every four rf-SQUIDs. Finally, the characteristic impedance of the overall structure was fine-tuned to achieve the standard value of 50 Ω in the low-frequency range (see Fig. 5(c)). This condition was pursued by incorporating interdigitate capacitors between the central strip line and the ground plane.

The die layout presented in Fig. 6(a) was obtained by arranging 110 supercells along a meandered coplanar waveguide having a total length of approximately 7 cm. Additionally, to mitigate noise stemming from vortex trapping in the superconductive ground plane, a matrix of vortex pinning sites was patterned on it [31], [32]. Twelve copies of the die were fabricated on a 2" wafer using standard shadow-mask UV-lithography processes. The oxidation process exploited for the realization of the thin insulating barrier of the Josephson junction was tuned to obtain a critical current for the junctions of around $I_c = 2$ μA. Fig. 6(b) and (c) show micrographs of one of the realized devices at different magnifications.

The fabricated device underwent testing in a dilution refrigerator equipped with a microwave measurement circuit inspired by the setup presented in [33]. The central components of this circuit are a pair of single-pole six-throw microwave switches located on the mixing chamber plate. Enabling the measurements of a set of calibration standards, these switches allow the shift of the reference planes of the measurement down to the ports of the device under test during a unique cooldown. For the measurement of the parametric amplifier, the referenced measurement circuit was slightly modified with the introduction of a pair of bias tees before each of the switches. This addition allowed for the use of a dc current as a bias parameter to tune the operating mode of the parametric amplifier.

In the 4–12 GHz measurement range allowed by the setup, the comparison between the behaviour of the biased amplifier and a reference thru highlighted the presence of bias-dependent internal losses and ripples within the device. These ripples are most

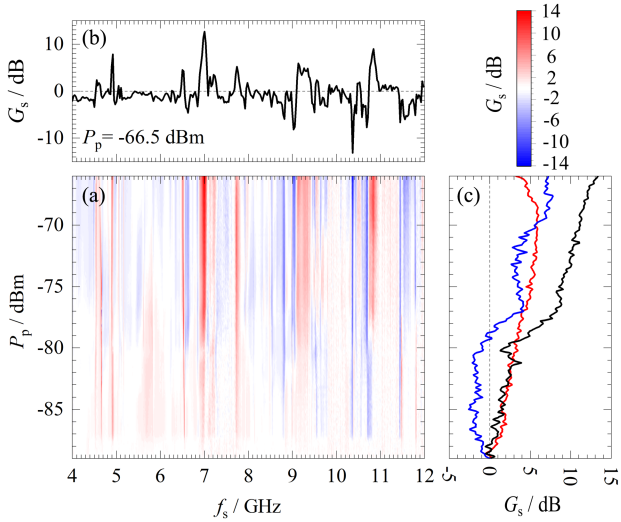

Fig. 7. (a) Measured pump-on-pump-off signal gain spectrum (G_s) in the 4–12 GHz range as a function of the pump power P_p. These latter values are referred to the input port of the DUT. (b) Line-cut representation of the pump-on-pump-off signal gain for a constant pump power $P_p = -66.5$ dBm. (c) Line cuts at three distinct signal frequencies (7.00 GHz for the black curve, 7.75 GHz for the red curve, and 10.80 GHz for the blue curve) illustrating different pump power dependencies of gain. The measurements were performed at 75 mK, with a fixed pump frequency f_p =18.0 GHz, a fixed bias current $I_{dc} = 9.71$ μA, and with a fixed input signal tone ($P_{input,s} = -20$ dBm) that correspond to a signal power at DUT level (P_s) that varies from −80 dBm to −100 dBm in the 4–12 GHz range.

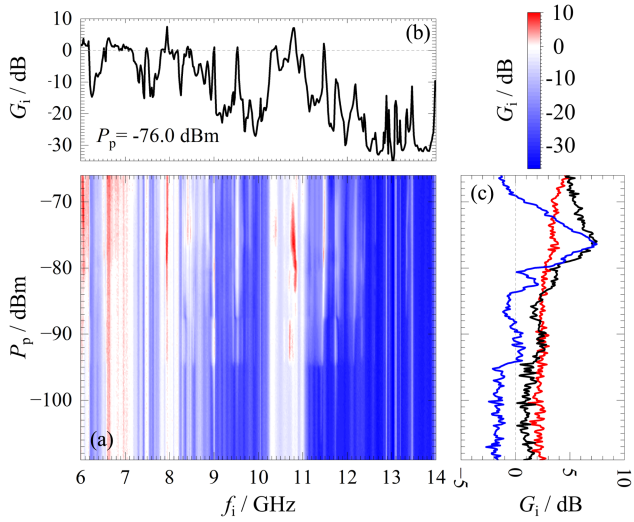

Fig. 8. (a) Measured three-wave mixing idler conversion gain spectrum (G_i) in the 6 to 14 GHz range as a function of the pump power P_p. (b) Line-cut representation at a constant pump power of $P_p = -76.0$ dBm. (c) Line cuts at three distinct idler frequencies (6.62 GHz for the red curve, 7.95 GHz for the black curve, and 10.80 GHz for the blue curve), illustrating different dependencies of the idler conversion gain on pump power. The measurements were performed in the same parameter space reported in the caption of Fig. 7.

likely related to JTWPA internal reflections due to impedance mismatches along the transmission line or to slot line modes, commonly excited in dense meandered structures. The detailed analysis of this behaviour is the subject of a paper currently under preparation. Interestingly, the device exhibited signatures of ongoing parametric down-conversion processes. These hallmarks can be emphasized by exploiting a pump-on-pump-off comparison which, as the name suggests, is the ratio between the power output of the pumped parametric amplifier and the power output when unpumped. It is important to emphasize that the use of this method for assessing amplifier performance, while useful, results in an overestimation of gain, especially in devices with significant internal losses.

Fig. 7(a) reports the signal gain spectrum evaluated by the pump-on-pump-off technique ($G_s = P_{s,pump-on}/P_{s,pump-off}$) as a function of the pump power (P_p), this latter evaluated at the DUT input port. The measurement was performed fixing the pump frequency at $f_p = 18.0$ GHz and the bias current at $I_{dc} = 9.71$ μA, a combination of parameters for which the device has exhibited the best performance. There, several spectral regions show gains greater than 0 dB (reaching values $G_s > 12$ dB) while others report a signal power reduction when this tone interacts with a strong pump. This effect can be attributed to the unprevented upconversion of the signal mode in the low-frequency bandwidth where the frequency dispersion is close to linear [34] combined to the rather high signal power used for the characterization that could potentially exceed the 1 dB compression point of the amplifier. Further investigation with a dedicated setup will quantify these particular aspects of the realized JTWPA. Analogously, Fig. 8(a) reports the idler conversion gain ($G_i = P_{i,pump-on}/P_{s,pump-off}$) [35], [36] evaluated in the same experimental parameters space. There, one can observe values exceeding 5 dB in various spectral regions, especially around the three-wave mixing idler frequencies corresponding to signal frequencies where G_s is non-negligible.

IV. Conclusion

We showed the development of a JTWPA, through a comprehensive process of design, simulation, and experimentation. The device exhibits significant signal gains and idler conversion factors across various frequency spectra. However, certain irregularities in gain were observed, potentially attributed to internal reflections in the JTWPA, probably due to impedance mismatches or slot line modes. While these phenomena require further investigation, the preliminary results presented in this study underscore the effectiveness of the JTWPA and its potential applicability across a wide range of quantum applications. Future research may focus on optimizing the JTWPA design and mitigating the observed irregularities.

ACKNOWLEDGMENT

Authors' Affiliations

L. Fasolo and L. Callegaro are with the INRiM - Istituto Nazionale di Ricerca Metrologica, I-10135 Turin, Italy (e-mail: l.fasolo@inrim.it).

F. Ahrens, A. Cian, D. Giubertoni, F. Mantegazzini, and B. Margesin are with Fondazione Bruno Kessler, Via Sommarive, I-38123 Trento, Italy, and also with INFN - TIFPA, Via Sommarive, I-38123 Trento, Italy.

G. Avallone, C. Barone, G. Carapella, V. Granata, C. Guarcello, and S. Pagano are with the Department of Physics, INFN -Gruppo Collegato Salerno, and CNR-SPIN Salerno Section, University of Salerno, 84084 Fisciano, Italy.

M. Borghesi, M. Faverzani, D. Labranca, R. Moretti, A. Nucciotti, L. Origo, M. Zannoni, and A. Giachero are with the Department of Physics, Piazza della Scienza, University of Milano Bicocca, I-20126 Milano, Italy, and also with INFN - Milano Bicocca, Piazza della Scienza, I-20126 Milano, ItalyINRiM - Istituto Nazionale di Ricerca Metrologica, I-10135 Turin, Italy.

A. P. Caricato, A. Leo, G. Maruccio, A. G. Monteduro, and S. Rizzato are with the INFN - Sezione di Lecce, I-73100 Lecce, Italy, and also with the Department of Physics, University of Salento, I-73100 Lecce, Italy.

I. Carusotto is with INO-CNR BEC Center, I-38123 Trento, Italy, and also with the Department of Physics, University of Salento, I-73100 Lecce, Italy.

A. D'Elia, D. Di Gioacchino, C. Gatti, C. Ligi, G. Maccarrone, A. S. Piedjou, L. Piersanti, A. Rettaroli, and S. Tocci are with the INFN - Laboratori Nazionali di Frascati, I-00044 Frascati, Italy.

P. Falferi and A. Vinante are with Fondazione Bruno Kessler, I-38123 Trento, Italy, also with INFN - TIFPA, I-38123 Trento, Italy, and also with IFN-CNR, I-38123 Trento, Italy.

E. Ferri is with INFN - Milano Bicocca, I-20126 Milano, Italy.

G. Filatrella is with Science and Technology Department, University of Sannio, 82100 Benevento, Italy, and also with INFN - Gruppo Collegato Salerno, 84084 Fisciano, Italy.

P. Livreri is with the Department of Engineering, University of Palermo, 90128 Palermo, Italy, and also with CNIT, RaSS, 56124 Pisa, Italy.

R. Mezzena is with the Department of Physics, University of Salento, I-73100 Lecce, Italy, and also with INFN - TIFPA, I-38123 Trento, Italy.

L. Oberto and E. Enrico are with the INRiM - Istituto Nazionale di Ricerca Metrologica, I-10135 Turin, Italy, and also with INFN - TIFPA, I-38123 Trento, Italy.

References

[1] J. Aumentado, "Superconducting parametric amplifiers: The state of the art in Josephson parametric amplifiers," *IEEE Microw. Mag.*, vol. 21, no. 8, pp. 45–59, Aug. 2020. [Online]. Available: https://api.semanticscholar.org/CorpusID:220466449

[2] L. Fasolo, A. Greco, and E. Enrico, "Superconducting Josephson-based metamaterials for quantum-limited parametric amplification: A review," in *Proc. Condensed-Matter Mater. Phys.*, 2019, pp. 72–92, doi: 10.5772/intechopen.89305.

[3] A. Giachero et al., "Detector array readout with traveling wave amplifiers," *J. Low Temp. Phys.*, vol. 209, pp. 658–666, 2022.

[4] S. Pagano et al., "Development of quantum limited superconducting amplifiers for advanced detection," *IEEE Trans. Appl. Supercond.*, vol. 32, no. 4, Jun. 2022, Art. no. 1500405.

[5] V. Granata et al., "Characterization of traveling-wave Josephson parametric amplifiers at t = 0.3k," *IEEE Trans. Appl. Supercond.*, vol. 33, no. 1, Jan. 2023, Art. no. 0500107.

[6] M. Borghesi et al., "Progress in the development of a KITWPA for the DARTWARS project," *Nucl. Instrum. Meth. A*, vol. 1047, 2023, Art. no. 167745.

[7] A. Rettaroli et al., "Ultra low noise readout with travelling wave parametric amplifiers: The DARTWARS project," *Nucl. Instrum. Meth. A*, vol. 1046, 2023, Art. no. 167679.

[8] C. Guarcello et al., "Modeling of Josephson traveling wave parametric amplifiers," *IEEE Trans. Appl. Supercond.*, vol. 33, no. 1, Jan. 2023, Art. no. 0600207.

[9] "Detector array readout with traveling wave amplifiers - Project site," 2021. [Online]. Available: https://dartwars.unimib.it/

[10] "Detector array readout with traveling wave amplifiers - European Commission," 2021, doi: 10.3030/101027746.

[11] L. Fasolo et al., "Josephson traveling wave parametric amplifiers as non-classical light source for microwave quantum illumination," *Meas.: Sensors*, vol. 18, 2021, Art. no. 100349. [Online]. Available: https://www.sciencedirect.com/science/article/pii/S2665917421003123

[12] F. Fesquet et al., "Perspectives of microwave quantum key distribution in the open air," *Phys. Rev. A*, vol. 108, Sep. 2023, Art. no. 032607. [Online]. Available: https://link.aps.org/doi/10.1103/PhysRevA.108.032607

[13] A. B. Zorin, "Josephson traveling-wave parametric amplifier with three-wave mixing," *Phys. Rev. Appl.*, vol. 6, Sep. 2016, Art. no. 034006. [Online]. Available: https://link.aps.org/doi/10.1103/PhysRevApplied.6.034006

[14] A. Greco, L. Fasolo, A. Meda, L. Callegaro, and E. Enrico, "Quantum model for RF-squid-based metamaterials enabling three-wave mixing and four-wave mixing traveling-wave parametric amplification," *Phys. Rev. B*, vol. 104, Nov. 2021, Art. no. 184517. [Online]. Available: https://link.aps.org/doi/10.1103/PhysRevB.104.184517

[15] K. O'Brien, C. Macklin, I. Siddiqi, and X. Zhang, "Resonant phase matching of Josephson junction traveling wave parametric amplifiers," *Phys. Rev. Lett.*, vol. 113, Oct. 2014, Art. no. 157001. [Online]. Available: https://link.aps.org/doi/10.1103/PhysRevLett.113.157001

[16] A. F. Roudsari et al., "Three-wave mixing traveling-wave parametric amplifier with periodic variation of the circuit parameters," *Appl. Phys. Lett.*, vol. 122, 2023, Art. no. 052601.

[17] A. Zorin, "Flux-driven Josephson traveling-wave parametric amplifier," *Phys. Rev. Appl.*, vol. 12, Oct. 2019, Art. no. 044051. [Online]. Available: https://link.aps.org/doi/10.1103/PhysRevApplied.12.044051

[18] T. Dixon, J. Dunstan, G. Long, J. Williams, P. Meeson, and C. Shelly, "Capturing complex behavior in Josephson traveling-wave parametric amplifiers," *Phys. Rev. Appl.*, vol. 14, Sep. 2020, Art. no. 034058. [Online]. Available: https://link.aps.org/doi/10.1103/PhysRevApplied.14.034058

[19] A. B. Zorin, "Quasi-phasematching in a poled Josephson traveling-wave parametric amplifier with three-wave mixing," *Appl. Phys. Lett.*, vol. 118, no. 22, 2021, Art. no. 222601, doi: 10.1063/5.0050787.

[20] M. Perelshtein et al., "Broadband continuous-variable entanglement generation using a Kerr-free Josephson metamaterial," *Phys. Rev. Appl.*, vol. 18, no. 2, 2022, Art. no. 024063, doi: 10.1103/PhysRevApplied.18.024063.

[21] Sonnet Software. [Online]. Available: https://www.sonnetsoftware.com/

[22] M. Esposito, A. Ranadive, L. Planat, and N. Roch, "Perspective on traveling wave microwave parametric amplifiers," *Appl. Phys. Lett.*, vol. 119, no. 12, 2021, Art. no. 120501, doi: 10.1063/5.0064892.

[23] A. D. O'Connell et al., "Microwave dielectric loss at single photon energies and millikelvin temperatures," *Appl. Phys. Lett.*, vol. 92, no. 11, 2008, Art. no. 112903, doi: 10.1063/1.2898887.

[24] S. Doyle, "Lumped element kinetic inductance detectors," 2008. [Online]. Available: https://orca.cardiff.ac.uk/id/eprint/54728/1/U585117.pdf

[25] M. S. Khalil, M. J. Stoutimore, F. C. Wellstood, and K. D. Osborn, "An analysis method for asymmetric resonator transmission applied to superconducting devices," *J. Appl. Phys.*, vol. 111, 2012, Art. no. 054510.

[26] A. Bruno, G. de Lange, S. Asaad, K. L. van der Enden, N. K. Langford, and L. DiCarlo, "Reducing intrinsic loss in superconducting resonators by surface treatment and deep etching of silicon substrates," *Appl. Phys. Lett.*, vol. 106, no. 18, 2015, Art. no. 182601, doi: 10.1063/1.4919761.

[27] A. Megrant et al., "Planar superconducting resonators with internal quality factors above one million," *Appl. Phys. Lett.*, vol. 100, pp. 11–14, 2012.

[28] C. R. H. McRae et al., "Materials loss measurements using superconducting microwave resonators," *Rev. Sci. Instrum.*, vol. 91, 2020, Art. no. 091101. [Online]. Available: http://aip.scitation.org/doi/10.1063/5.0017378

[29] T. Noguchi, A. Dominjon, M. Kroug, S. Mima, and C. Otani, "Characteristics of very high Q Nb superconducting resonators for microwave kinetic inductance detectors," *IEEE Trans. Appl. Supercond.*, vol. 29, no. 5, Aug. 2019, Art. no. 2400205.

[30] C. Kissling et al., "Vulnerability to parameter spread in Josephson traveling-wave parametric amplifiers," *IEEE Trans. Appl. Supercond.*, vol. 33, no. 5, Aug. 2023, Art. no. 1700106.

[31] I. Nsanzineza and B. L. Plourde, "Trapping a single vortex and reducing quasiparticles in a superconducting resonator," *Phys. Rev. Lett.*, vol. 113, no. 11, 2014, Art. no. 117002.

[32] B. Chiaro et al., "Dielectric surface loss in superconducting resonators with flux-trapping holes," *Supercond. Sci. Technol.*, vol. 29, no. 10, pp. 1–5, 2016.

[33] L. Ranzani, L. Spietz, Z. Popovic, and J. Aumentado, "Two-port microwave calibration at millikelvin temperatures," *Rev. Sci. Instrum.*, vol. 84, 2013, Art. no. 034704.

[34] H. Renberg Nilsson, A. Fadavi Roudsari, D. Shiri, P. Delsing, and V. Shumeiko, "High-gain traveling-wave parametric amplifier based on three-wave mixing," *Phys. Rev. Appl.*, vol. 19, Apr. 2023, Art. no. 044056. [Online]. Available: https://link.aps.org/doi/10.1103/PhysRevApplied.19.044056

[35] L. Fasolo et al., "Bimodal approach for noise figures of merit evaluation in quantum-limited Josephson traveling wave parametric amplifiers," *IEEE Trans. Appl. Supercond.*, vol. 32, no. 4, Jun. 2022, Art. no. 1700306.

[36] M. Malnou, T. Larson, J. D. Teufel, F. Lecocq, and J. Aumentado, "Low-noise cryogenic microwave amplifier characterization with a calibrated noise source," 2023, *arXiv:2312.14900*.

Open Access funding provided by 'Istituto Nazionale di Ricerca Metrologica - INRiM' within the CRUI CARE Agreement